Fabrication and testing of the 3.5 m, f/1.75 WIYN primary mirror.

D. Anderson, J. Burge, D. Ketelsen, B. Martin, S. West
Steward Observatory Mirror Laboratory
University of Arizona
Tucson, Arizona 85721

G. Poczulp, J. Richardson, W. Wong
National Optical Astronomy Observatories
P.O. Box 26732, Tucson, Arizona 85726-6732

1. Abstract.

The continuing development of rapid fabrication methods for large optics at the Steward Observatory Mirror Lab has resulted in the completion of the WIYN 3.5 m primary mirror in only five months. The use of these methods, though rapid, also resulted in one of the best surface figures we have produced (16 nm rms), excellent microroughness (8 angstroms rms), and very smooth small-scale figure error as determined by the structure function of the surface errors. In this paper, we review the important techniques in the grinding, polishing, and testing of the mirror used to achieve these results.

2. Introduction.

2.1 Mirror design.

The WIYN telescope is a 3.5 m. Ritchey-Chrétien design with an f/1.75 hyperboloidal primary mirror with a conic constant of -1.0708. The primary mirror blank is an Ohara E6, borosilicate, lightweight casting formed in the giant rotating furnace at the Steward Observatory Mirror Lab. Rotation of the furnace during casting allows the liquid glass forming the approximately 28 mm thick faceplate of the mirror to be spun into a curve of very nearly the correct radius of curvature. This eliminates the enormous effort of generating in a curve having 122 mm of sag, not to mention the time and risk involved in annealing such a thick faceplate. Blanks up to 6.5 m. in diameter have been cast using this process.

The blank's honeycomb internal structure incorporates 294 hexagonal cores having a "diameter" of about 175 mm. The walls of the honeycomb are approximately 12 mm thick and both the faceplate and the backplate are about 28 mm thick. The center hole has a diameter of just under 1 m.

2.2. Initial work.

Following the casting, the mirror blank went to the optical shop at NOAO where it was generated, etched, ground, and polished to a good sphere. Extensive testing followed to evaluate the thermal behavior of the mirror as well its mechanical response in the telescope cell where the mirror is supported on 66 active supports. After the initial asphérization at the Mirror Lab with the mirror on a different support the mirror was returned to the telescope cell for final figuring. The active supports during final figuring were replaced with passive supports at the same locations as the active supports. Small differences in the two supports will be removed with the active support system in the telescope.

3. Aspherization

3.1. Stressed-lap grinding.

To introduce the required 171 microns of asphericity from best-fit sphere in a smooth fashion we utilized the unique capabilities of the stressed-lap polisher as a grinding tool.[1,2] Using the stressed-lap as a grinding tool had

0-8194-1243-0/94/$6.00

been done earlier on the SOR 3.5 m. primary mirror to remove 13 microns of trefoil error introduced during the generating of the asphere. That case was somewhat different since the grinding tool was working on a fully aspherized surface. In WIYN's case the tool needed to start from a sphere and progress through to the final asphere since the correction was not generated in. To introduce the aspheric correction in a smooth way the grinding tool needs to fit the surface of the developing asphere whose conic is changing. The stressed-lap grinding tool is ideal for this since the lap can take on the shape of any conic from a sphere (K = 0) to the final asphere (K = -1.0708) within the accuracy of its mechanical limitations, typically on the order of a few microns rms.

For the WIYN aspherization we used the 1.2 m. diameter stressed-lap with a 1 m diameter area of working surface. The 100 mm square pitch pads were covered with .5 mm thick layer of Zinc metal grinding pads commonly used in the ophthalmic industry. These pads have a self adhesive backing that readily sticks to the pitch. This Zinc-on-pitch tool can be pressed against the mirror at regular intervals giving the lap the required initial shape having a particular conic constant. The lap is then actively deformed from this shape as it rotates and traverses the mirror during the grinding stroke always closely matching the shape of the mirror.

The diameter of the tool was chosen to introduce the asphere as efficiently as possible from the best-fit sphere. This requires that the tool lap the center and edge equally leaving the .7 zone relatively untouched. A 1 m diameter tool was chosen along with two separate machine strokes, one that worked the center and one the edge. With this single tool we were able to aspherize the mirror in only 92 hours of machine time. In Figure 1 is shown a 10.6 micron interferogram of the surface after 10 hours of grinding. The sum of the two strokes clearly was introducing the spherical aberration very smoothly. By adjusting the relative time spent on the center stroke *vs* the edge stroke we could maintain close control over the vertex radius of curvature.

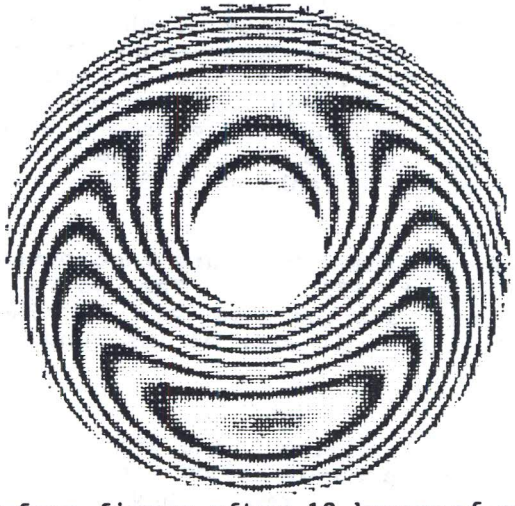

Figure 1. The surface figure after 10 hours of grinding.

Two sizes of aluminum oxide abrasive was used for the grinding. We started with 15 micron abrasive until 75% of the correction was in, then switched to 9 micron abrasive to finish. We felt using a finer abrasive carried a greater risk of scratching.

3.2. IR testing.

To monitor the aspherization we used a 10.6 micron interferometer in two different ways. Initially, we needed to monitor the figure as we were grinding in the asphere up to the point where we could effectively use an IR null lens. Since the modulation of the IR fringes imaged on a pyroelectric vidicon falls off rapidly with increasing fringe density the null lens could only be used within

about 25 microns of the final asphere.

For the bulk of the aspherization we used the IR interferometer in a zonal slope test similar to the wire test. This type of test measures the longitudinal spherical aberration in the mirror by locating the intersections of surface normals with the optical axis. As in a wire test, a bar is placed across the mirror diameter with equally spaced pins marking zones in the pupil. Because of increased diffraction at 10.6 microns the normal narrow pins were replaced with 50 mm wide strips of paper every 250 mm across the pupil. A diverger producing a good spherical wavefront was used with the IR interferometer to produce interference fringes of the highly aspheric surface. The diverger was positioned such that the fringes were "in focus" at one of the zones marked by the paper strips, i.e., the slope of the spherical wavefront matches that of the aspheric surface at the chosen zone. Figure 2 depicts the image viewed in the interferometer. By measuring the distance from the mirror's vertex to the diverger focus for several zones and knowing the position of the zones the radius and conic constant of the mirror can be determined. In practice only one radius distance was measured for a single starting zone (usually the one nearest the center) and the differential motion of the diverger for the remaining zones was measured.

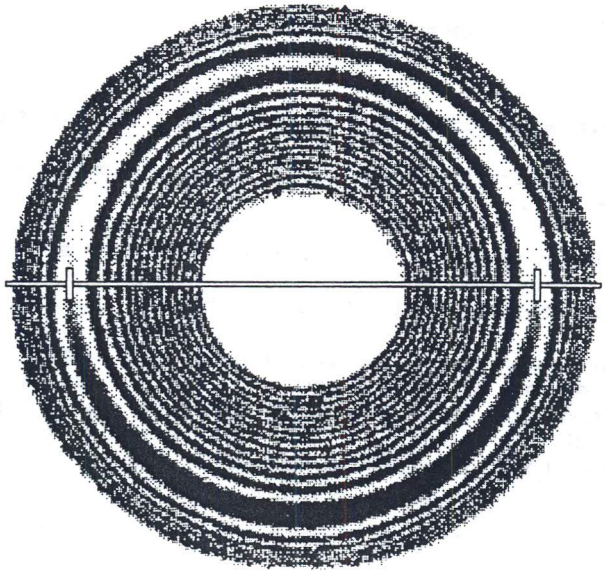

Figure 2. A synthetic image of the IR zonal test. In actual use only a few fringes near the null fringe are visible.

A computer program was written to perform the data analysis for this test. A least-squares fit was used to determine the vertex radius of curvature R and conic constant K of the mirror. The residual slopes are then calculated and integrated to show errors in the surface height.

The height of intersection of the normal rays with the axis is described, to an excellent approximation, by the equation:

$$Z = R - \frac{Kr^2}{2R}$$

where Z = distance from the mirror vertex to zonal center of curvature.

R = mirror's vertex radius of curvature.

r = radial position of zone

K = mirror's conic constant

A single data set will contain two variables, x_i the radial pin position and Z_i the height of the normal intercept above the mirror vertex. The corresponding radial position of the mirror r_i is obtained by projecting the known pin (paper strip) positions from the bar to the optical surface.

To find *R* an *K*, a least squares fit using singular value decomposition[3] finds the coefficients a_0 and a_2 for the function

$$Z = a_0 + a_2 r^2$$

where

$$R = a_0$$

$$K = -2Ra_2$$

After fitting a_0 and a_2 to the data, the residual slope errors are calculated and integrated to give the residual surface errors. The surface slope, defining positive slope errors as causing an increase in Z, is obtained from the relationship

$$\delta\theta = \frac{r\Delta Z}{(Z - sag)^2 + r^2}$$

where $\delta\theta(r)$ = surface slope deviation from ideal conic.

ΔZ = residual longitudinal spherical aberration ($Z_{data} - Z_{fit}$).

sag = surface shape given by the conic equation.

The surface errors are calculated by integrating $-\delta\theta(r)$ using Simpson's rule.

The data and the polynomial fit for a test are shown in Figure 3a. At this stage in the fabrication the surface had over 100 microns peak-to-valley departure from the best-fit sphere. The best fit conic at this point is given by R = 12287.5 mm and K = -0.654. The integration of these data gives the surface departure from this conicoid, shown in Figure 3b.

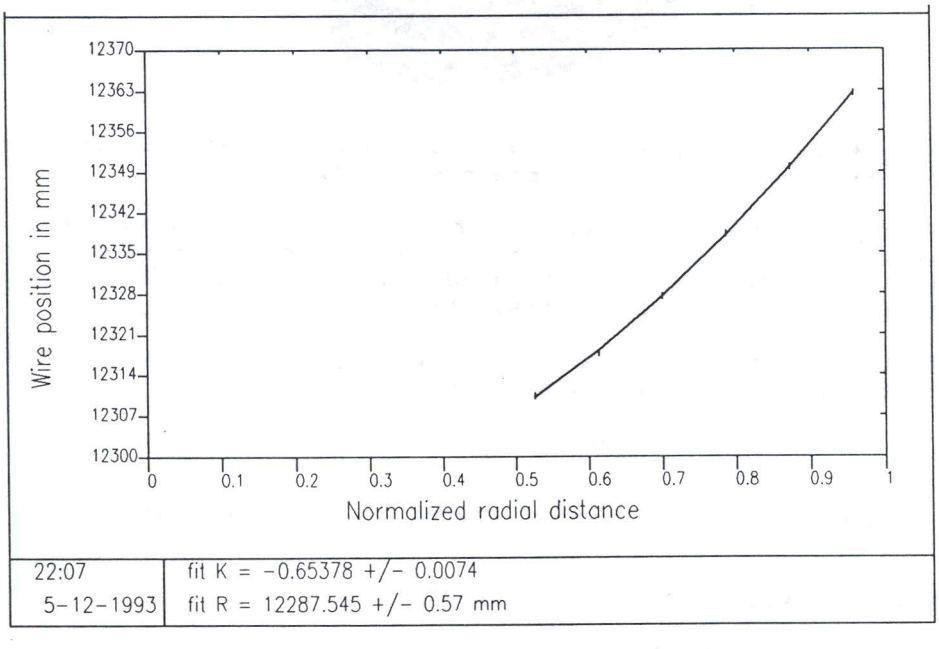

Figure 3a. The data and polynomial fit to the data of the IR zonal test.

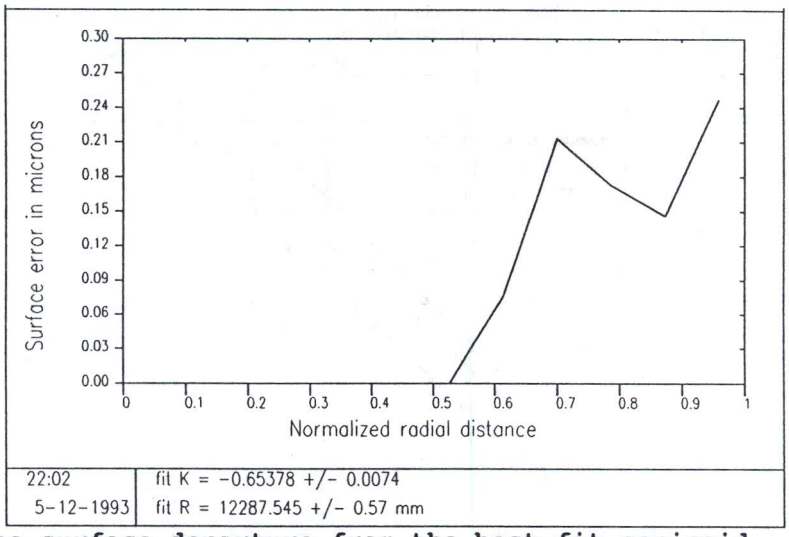

Figure 3b. The surface departure from the best-fit conicoid.

After approximately 85% of the aspheric departure had been introduced, an IR null lens, constructed at NOAO, was attached to the IR interferometer and direct phase measurements of the surface could be made. Figure 4 is a synthetic interferogram from phase data taken on 10-21-92 when the conic was -.97 and a complete data set could be obtained with the phase measuring interferometer. It is evident, based on this interferogram, that the stressed lap, in a period of less than four weeks, introduced the majority of the asphere in a very smooth fashion.

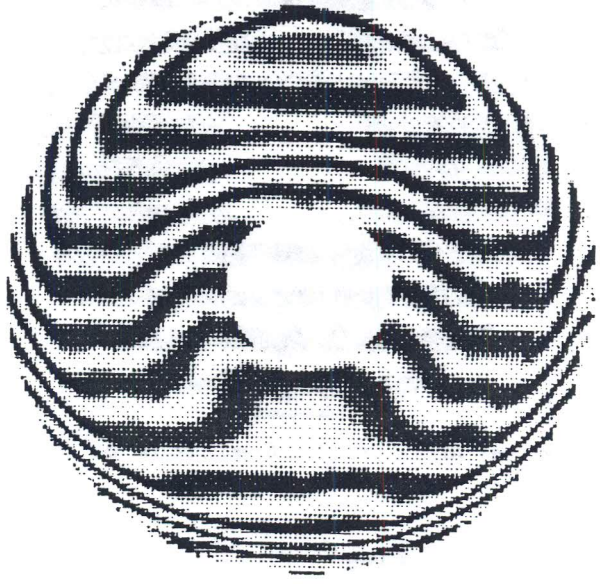

Figure 4. A synthetic interferogram from IR phase data taken through the null lens just after installation.

Shown in Figure 5 is a plot of the vertex radius of curvature *vs* the conic constant during the asphericization. The radius of the initial sphere was long by about 8 mm at the start requiring a bit more work in the center to "pull" the radius in towards the desired final vertex radius by the time the asphere was introduced. The mirror's radius ended about 4 mm long but well within the specification. The entire asphericization process based on the IR measurements took 8 weeks with a total of 92 hours of machine time. Figure 6 shows a phase map and interferogram of the surface at the end of grinding with the surface at .29 microns rms.

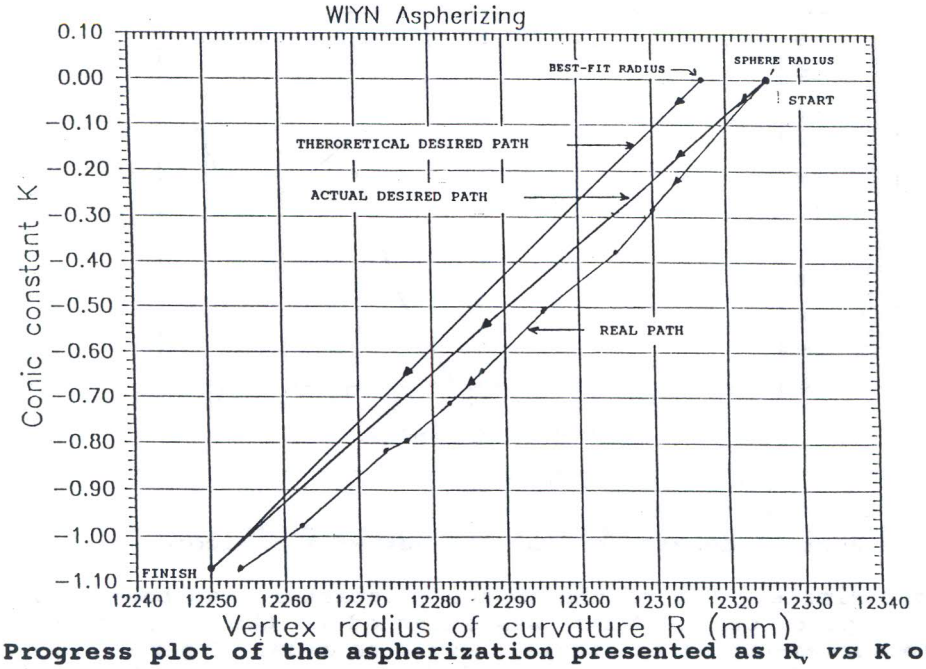

Figure 5. Progress plot of the aspherization presented as R_v *vs* K of the best fit conicoid.

Figure 6. A synthetic interferogram at 10.6 microns of the surface at the end of grinding.

4. Polishing

4.1. Initial polishing.

Initial polishing concentrated on maintaining the figure already achieved and obtaining a specular surface for visible testing. Following 10 hours of polishing a final IR test was performed and the visible null lens installed and an initial phase measurement made. In Figure 7 is shown a comparison of the two tests. In (a) the final IR data has been rescaled to waves at 633 nm, the same as the visible phase map shown in (b). The surface errors measured in the IR are somewhat higher than the visible due mainly to the center being better imaged in the visible and less high frequency noise in the visible. The high frequency error in the IR tests result from index inhomogeneities in the germanium lenses appearing as streaky features. Given the relatively close agreement between the

two results work proceeded with the visible null lens as guide.

(a)

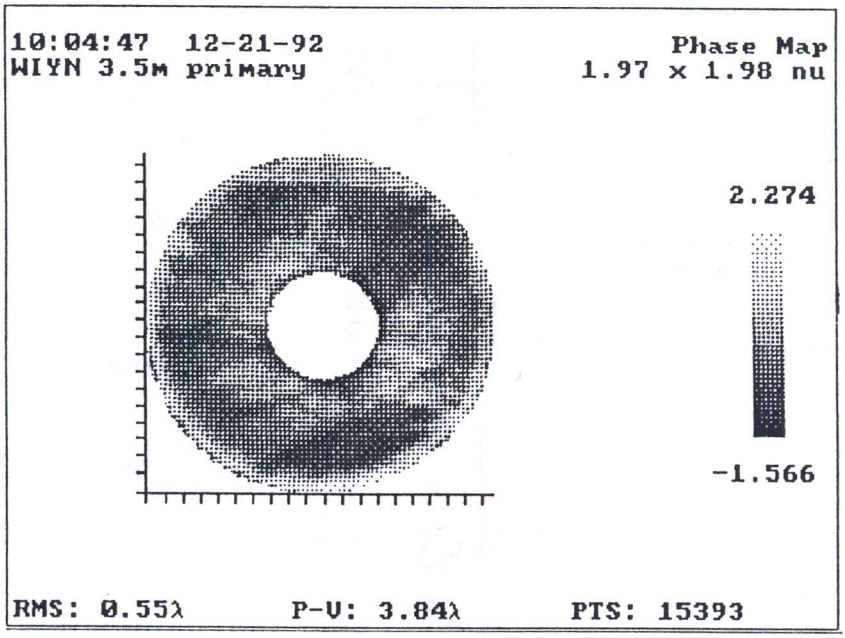

(b)

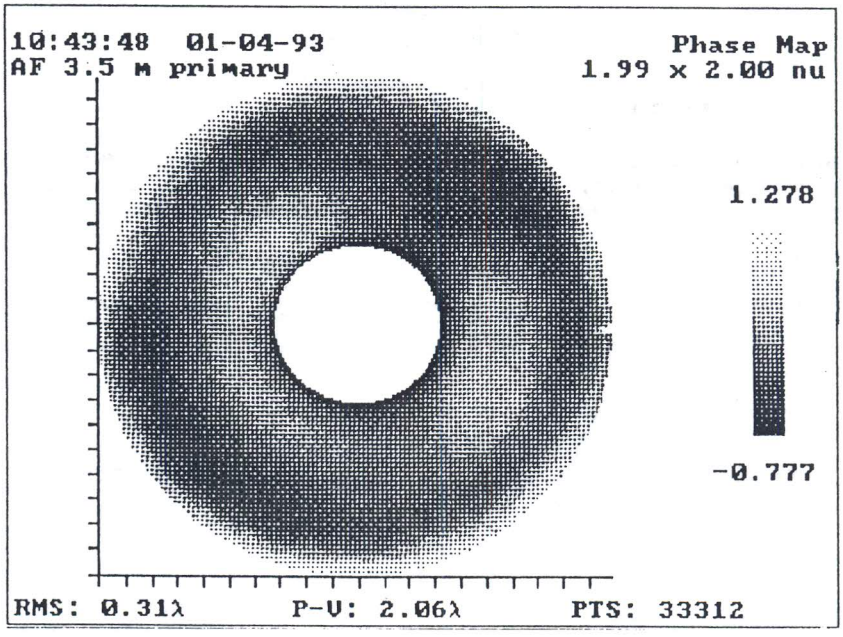

Figure 7. A comparison of the last IR test data and the first visible test data. In (a) the data taken at 10.6 microns has been rescaled to waves at 633 nm, the same as in (b).

4.2. The null lens.

A schematic of the null lens/interferometer assembly is shown in Figure 8. The main parts of the unit are a phase-measuring Shack cube interferometer, refractive Offner null corrector, CCD camera and relay optics, Invar frame, adjustable kinematic lens mounts, high precision rotary table, and a remote controllable 5-axis positioner. The Invar frame provides for +/- 5 degree C temperature tolerance for the axial spacings.

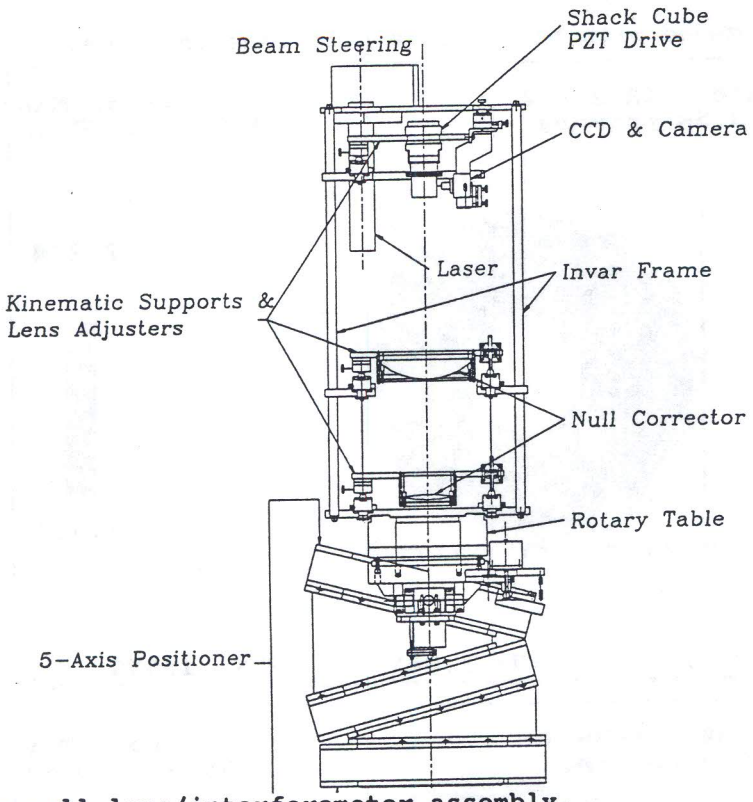

Figure 8. The null lens/interferometer assembly.

Figure 9 shows the optical layout of the Offner null lens consisting of a Shack cube, a large relay lens, and a smaller field lens. The lens surfaces and spacings were optimized to give a reflected wavefront error of .003 waves rms at 633 nm.

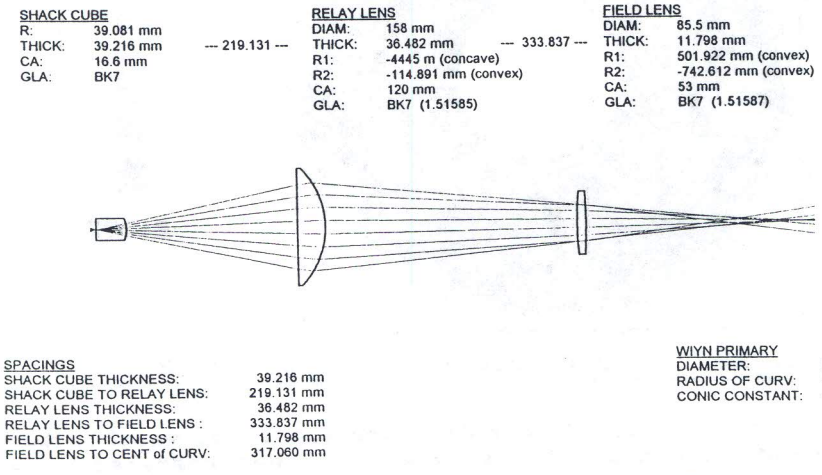

Figure 9. The optical layout of the null lens/interferometer.

A thorough tolerance analysis of the null lens was performed to determine the precise relationship between uncertainties in the null lens and specific errors in the primary mirror such as conic constant error and surface irregularities with the conic error removed. Because the telescope allows for a small correction of conic constant error (equivalently, third-order spherical aberration), it was separated from the other errors.

Table 1 gives a detailed list of the null lens parameters and their uncertainties, which lead to an estimated uncertainty in the conic constant K of 0.00012 and an uncertainty in the wavefront of .046 waves rms. An error budget created for each parameter of the test optics is shown. These errors are added in quadrature to give the rms estimate of the system measurement errors.

		Final Measured Parameters			
		Actual		Conic	Wavefront
	units	value	uncertainty	uncertainty	RMS
Shack Cube:					
Thickness	mm	39.216	0.006	0.000035	0.0006
Radius 2	mm	-39.081	0.005	0.000029	0.0005
Irregularity (rms)	waves	0.005	0.005		0.0141
Runout 2	μm		5	0.000000	0.0003
Airspace	mm	219.131	0.003	0.000017	0.0003
Relay Lens:					
Curvature 1	/mm	2.36E-07	1.00E-08	0.000002	0.0000
Thickness	mm	36.482	0.005	0.000020	0.0004
Radius 2	mm	-114.891	0.012	0.000043	0.0010
Irregularity 1 (rms)	waves	0.014	0.002		0.0146
Irregularity 2 (rms)	waves	0.014	0.011		0.0184
Index		1.51585	1.00E-05	0.000030	0.0002
Inhomogeneity	rms		2.50E-7		0.0288
Runout 1	μm		4		0.0009
Runout 2	μm		4		0.0006
Airspace	mm	333.837	0.003	0.000014	0.0005
Field Lens:					
Radius 1	mm	501.922	0.012	0.000020	0.0011
Thickness	mm	11.798	0.005	0.000001	0.0002
Radius 2	mm	742.612	0.014	0.000010	0.0007
Irregularity 1 (rms)	waves	0.016	0.002		0.0166
Irregularity 2 (rms)	waves	0.013	0.002		0.0136
Index		1.51587	1.00E-05	0.000027	0.0013
Inhomogeneity	rms		2.50E-07		0.0093
Runout 1	μm		3	0.000000	0.0012
Runout 2	μm		3	0.000000	0.0014
Residual Wavefront Error:	rms			0.000000	0.0030
Primary Radius	mm	12253.5	0.5	0.000043	0.0001
Worst Case				**0.000292**	**0.1297**
RSS				**0.000094**	**0.0463**

Table 1. Tolerance analysis for the null lens/interferometer.

While the measured values of the null lens parameters give an estimated uncertainty in K well within the specified uncertainty of +/- 0.0007, any errors made in those measurements could lead to a serious error being made in the conic if undetected. Therefore, an independent measurement of the null lens was made with the system *in situ* using a computer generated hologram (CGH).[4,5,6] The holographic method provides an independent verification of the conic constant as well as an easy means of determining the non-axisymmetric errors in the null lens.

In the CGH null lens test a hologram of the mirror is tested by the null lens. The hologram is made so it will appear to the null lens as if it were a perfect primary mirror. The hologram is simply a circular grating or zone plate. It is made of concentric grooves etched into a very flat piece of fused silica coated with a thin film of aluminum. The grooves are fabricated using electron-beam lithography developed for the production of integrated circuits. The spacing of the grooves defines the mirror surface that the hologram replaces. The groove depth and width are optimized to minimize fabrication costs while giving the correct intensity of diffracted light.

A layout of the CGH null test, shown in Figure 10, depicts the null lens and CGH. No modifications are made to the null lens to perform the test. The null corrector tests the hologram exactly as if it were the real finished mirror. The CGH is positioned in the caustic such that the paraxial focus of the null lens is at the surface of the hologram. Once the hologram is near the correct position, the shape of the fringes from the interferometer is used to align the hologram in exactly the same way as the primary mirror itself.

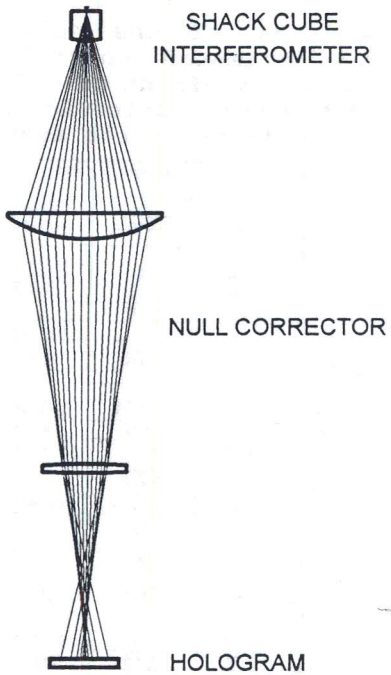

Figure 10. The hologram is positioned at the paraxial focus of the null lens and aligned in the same way as the primary mirror with the 5-axis mount on the null lens assembly.

The null lens errors were determined by measuring the CGH with the null lens and subtracting known errors in the CGH. These known errors in the CGH are caused by errors in the surface figure of the CGH substrate and by small differences between the CGH design and the final mirror. The magnitude of third-order spherical aberration caused by these errors was 57 nm peak-valley. These errors were calculated using Zernike polynomials and corrected for the imaging distortion in the null lens before being subtracted from the test results.

To separate azimuthal errors in the CGH from those in the null lens the CGH was measured at 15 equally spaced azimuthal orientations. The results were averaged to eliminate hologram errors up to 15th order while the errors in the null lens remain. The results of this average are shown in Figure 11a. Shown in Figure 11b is the result of this measurement after subtracting the known CGH errors described above. These errors were then subtracted from the mirror test data as test optic errors. Note that the residual spherical aberration in the null lens measurement is very small (Z_8=-.003 waves) indicating an extremely well made null lens.

(a)

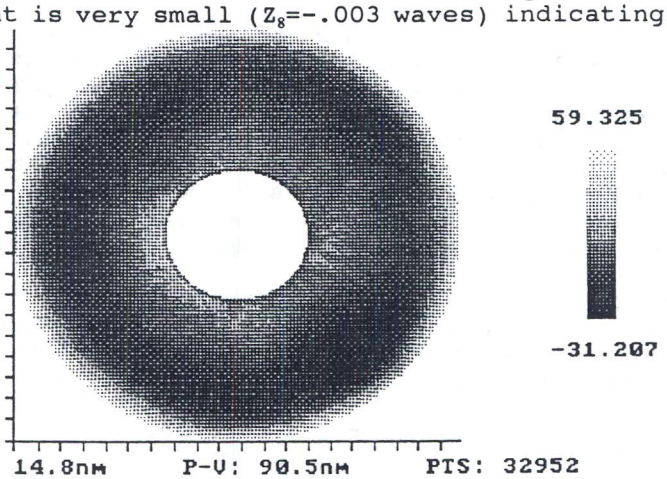

(b)

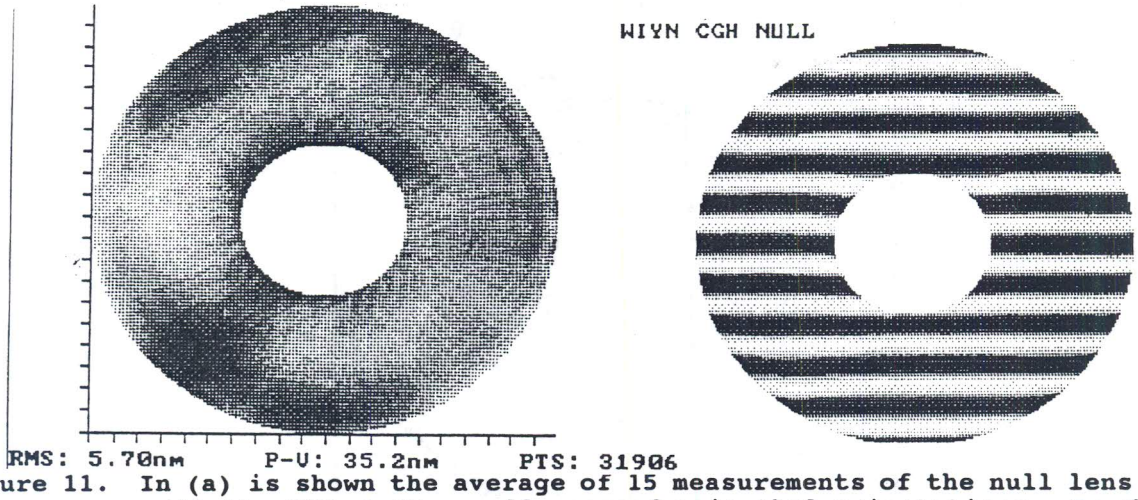

Figure 11. In (a) is shown the average of 15 measurements of the null lens made with the CGH at 15 equally spaced azimuthal orientations. In (b) is shown the same data with known CGH errors subtracted.

4.3. Mirror pressurization during polishing.

One of the problems encountered when polishing any structured mirror is the quilting or "print-through" of the cellular structure into the surface figure caused by a deformation of the unsupported area of each cell with respect to the cell walls as the polishing tool passes over the cell. The deformation leads to increased polishing pressure at the cell boundaries with respect to the cell center leading to bumps forming over the cell after the tool passes by. In Figure 12a is shown a phase map of the mirror just after the polish out stage where a pressure of about .5 psi had been used and where the resulting quilting is quite large (the phase data has 36 Zernike terms removed to show only high frequency errors). Figure 12b is a contour plot of the average cell showing the shape and magnitude of the quilting, units are in nanometers with a peak-valley of 44 nm.

(a)

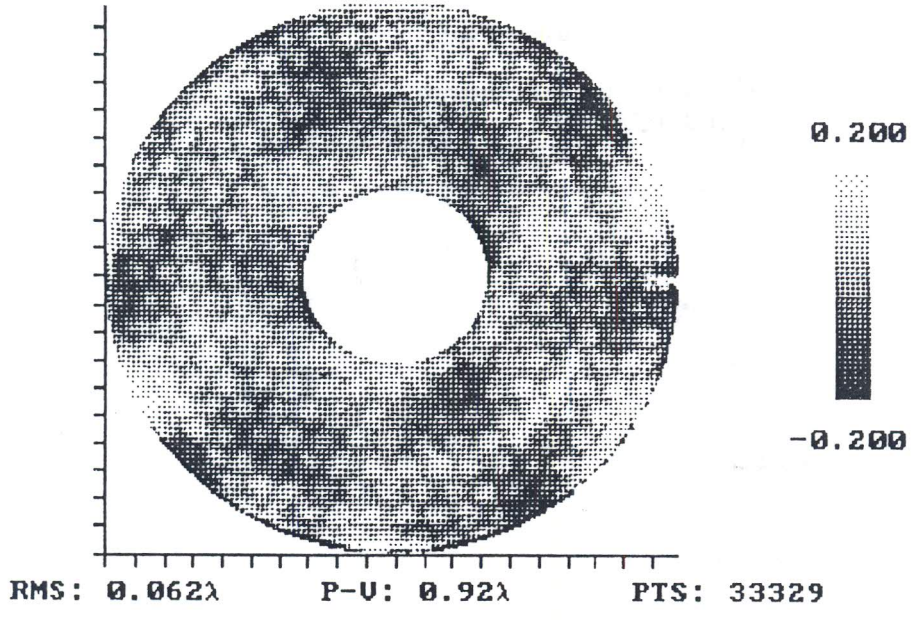

(b)

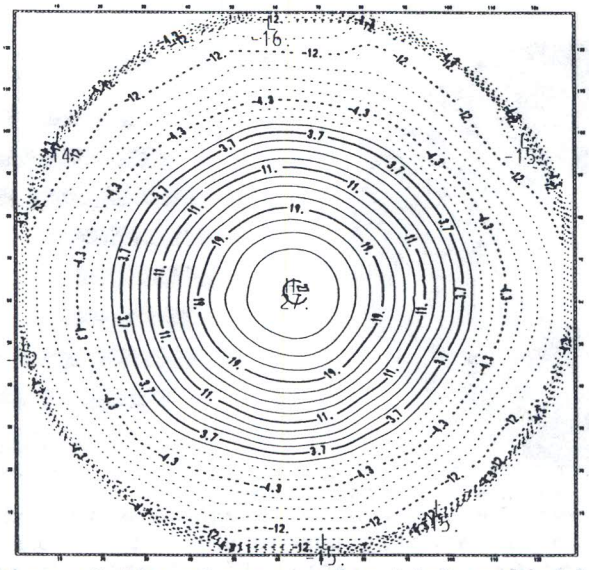

Figure 12. The quilting of the mirror under high polishing loads during polishing is shown in (a) and a contour plot of the surface figure over the average cell is shown in (b).

The simplest way to reduce this effect is to use very light polishing pressures resulting in small deflections. However, with large, heavy polishing tools off-loading the tool so that only a few percent of its weight is used in polishing is difficult. For the WIYN mirror we implemented a pressurization system whereby the internal structure of the mirror is pressurized by just the amount required to provide a balancing force to the polishing tool. The system is shown schematically in Figure 13. Initial tests were performed to confirm that the mirror did not deform in any way that would be imprinted by the 1 m diameter polishing tool. At a typical polishing/pressurization pressure of .2 psi the principal deformation of the mirror was about .4 waves of astigmatism with no significant high order bending. The subdiameter polishing tool rides over low order errors without imprinting them.

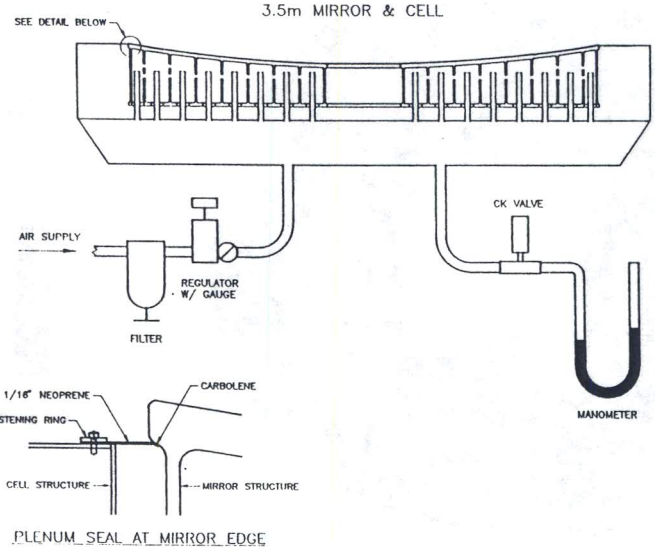

Figure 13. The pressurization system.

The pressurization system was used during polishing and turned off when testing. The results of this method were quite dramatic with the quilting being reduced by a factor of 7 as shown in Figure 14. The final phase map with 36 Zernike terms removed is shown in (a) and the average cell contour plot is shown in (b). At 6 nm peak-valley the quilting is quite negligible in the performance of the mirror in the telescope.

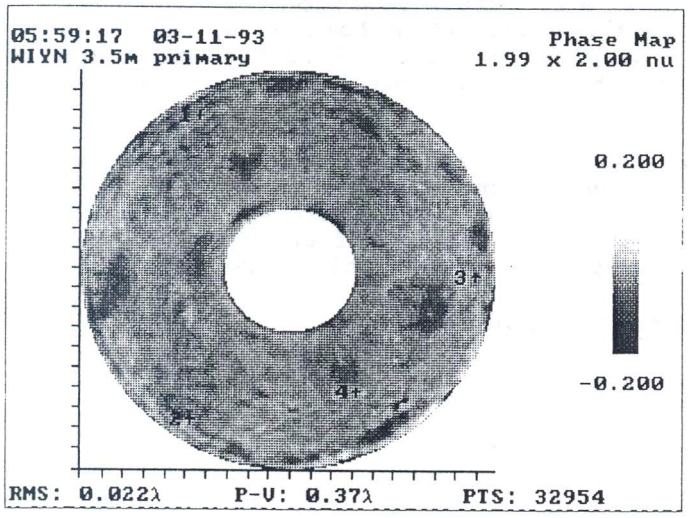

(a)

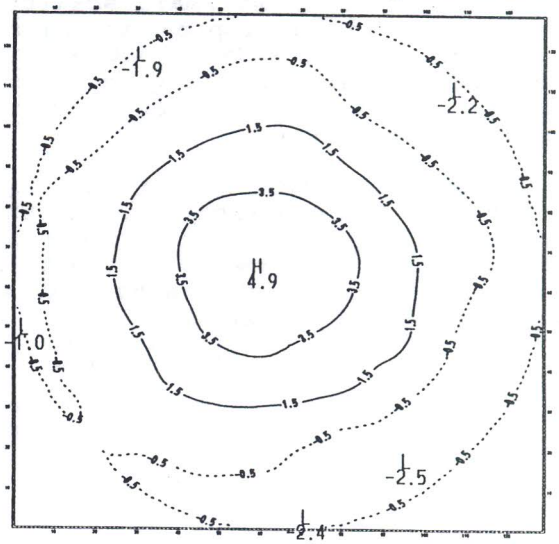

(b)

Figure 14. (a) The final phase map with 36 Zernike terms removed. (b) A contour plot of the average cell.

5. Final test results.

Figure 15a is a map of the surface errors of the finished mirror. The figure error is dominated by astigmatism resulting from a slight change in support forces during final testing that we could not fully remove. The active telescope support will easily compensate for this small error. Figure 15b is a map of the mirror with this astigmatism removed. The final figure quality over the surface of the clear aperture is 15.8 nm rms.

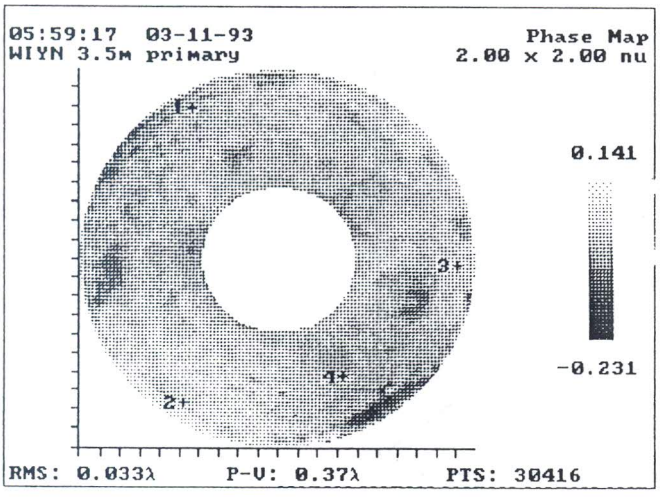

(a)

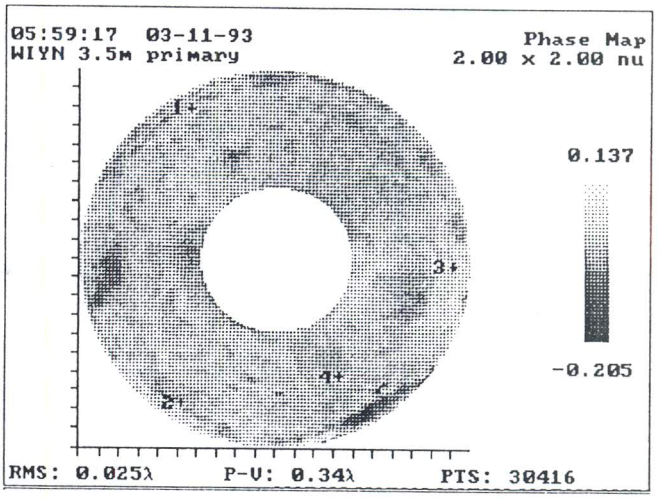

(b)

Figure 15. The final test data with astigmatism in (a) and out (b).

The specification stated in the contract was originally for a seeing-limited structure function[7] corresponding to .125 arc second FWHM seeing at 500 nm covering the middle range of spatial scales, an rms wavefront difference of 71 nm at large spatial scales, and an allowance for a loss of up to 5% of light at 500 nm due to small scale figure errors, corresponding to an rms wavefront difference of 25 nm at small scales. Upon reaching that specification it was agreed to continue to improve the mirror until a structure function corresponding to .09 arc seconds FWHM at 500 nm with an allowance for a loss of up to 3% of light due to small scale figure errors. The plot in Figure 16 is the structure function of the final data over the clear aperture plotted with the two specification curves.

To date, not only is this the highest quality mirror produced by the Mirror Lab but also the one fabricated in the shortest amount of time. Figure 17 is a plot of figure progress *vs* time for this project. The entire project from start to finish took just over 5 months to complete. The ability of the stressed-lap to rapidly grind in the asphere as well as polish it smoothly accounts for a large measure of our success.

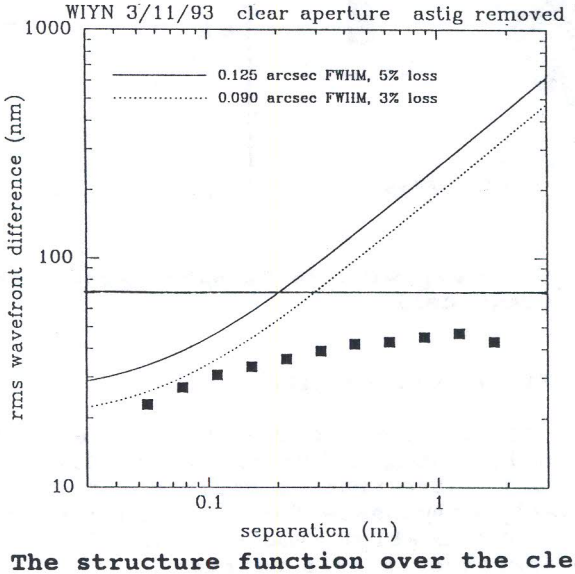

Figure 16. The structure function over the clear aperture.

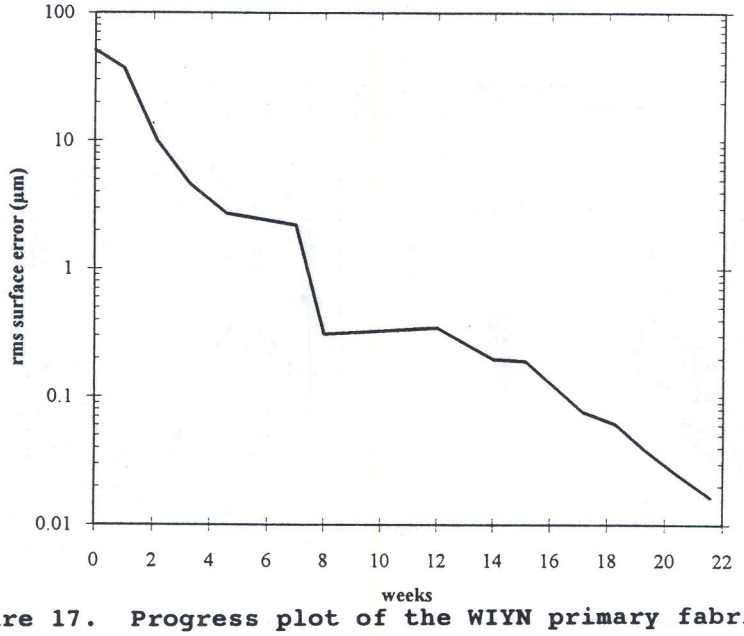

Figure 17. Progress plot of the WIYN primary fabrication.

References

1. H.M.Martin, D.S.Anderson, J.R.P.Angel, R.H.Nagel, S.C.West, and R.S.Young, "Progress in the Stressed-lap Polishing of a 1.8 m f/1 Mirror", *Advanced Technology Optical Telescopes IV*, ed. L.Barr, Proc. SPIE 1236, p.682, (1990).

2. H.M.Martin, D.S.Anderson, J.R.P.Angel, J.H.Burge, W.B.Davison, S.T.DeRigne, B.B.Hille, D.A.Ketelsen, W.C.Kittrell, R.McMillan, R.H.Nagel, T.J.Trebisky, S.C.West, and R.S.Young, "Stressed-lap Polishing of 1.8-m f/1 and 3.5-m f/1.5 Primary Mirrors', *Proc. ESO Conference on Progress in Telescope and Instrumentation Technologies*, ed. M.H.Ulrich, p.169 (1992).

3. W.H.Press, B.P.Flannery, S.A.Teukolsky, W.T.Vetterling, *Numerical Recipes in C*, Cambridge University Press, 1988.

4. J. H. Burge, "A null test for null correctors: error analysis," in Quality and Reliability for Optical Systems, J. W. Bilbro and R. E. Parks, eds., Proc. SPIE 1993, in press (1993).

5. J. H. Burge, "Certification of null correctors for primary mirrors," in Advanced Optical Manufacturing and Testing IV, J. Doherty, ed., Proc. SPIE 1994, in press (1993).

6. J. H. Burge, Advanced Techniques for Measuring Primary Mirrors for Astronomical Telescopes, Ph. D. Dissertation, Optical Sciences, University of Arizona (1993).

7. J.M.Hill, "Optical Design, Error Budget and Specifications for the Columbus Project Telescope", *SPIE Vol. 1236 Advanced Technology Optical Telescopes IV*, (1990).